ODS ALLOY DEVELOPMENT

I. G. Wright, B. A. Pint, and C. G. McKamey
Oak Ridge National Laboratory

INTRODUCTION

The overall goal of this project is to facilitate the exploitation of oxide dispersion-strengthened (ODS) alloys. The main barriers to the wider use of these alloys are the fact that they cannot be joined by conventional techniques; they have highly-directional mechanical properties: in particular, for extruded tubes with present processing the creep strength in the transverse direction typically is significantly lower than that in the axial direction; these alloys have unusual mechanical behavior, in that their high sensitivity to strain rate results in a mode of creep failure that is different from conventional high-temperature alloys; and, because a powder metallurgical route is required for their fabrication, these alloys are expensive.

There are several options being explored to overcome these barriers. For joining, unconventional approaches including inertia welding and transient liquid phase (TLP) bonding are being examined. For modification of the mechanical properties, innovative processing routes are being explored that have the potential to produce the desired microstructure. In addition, the alloy properties and characteristics are being quantified, where possible, so that there are no surprises for designers and engineers looking to use these alloys.

Approaches taken in this project involve studies to understand and quantify all available routes for joining these alloys, including the cases where it is unlikely that the joints will exhibit a very high fraction of the original metal strength. Other studies are aimed at developing a mechanistic understanding of how to control the alloy microstructure, so that the necessary parameters can be readily translated from laboratory to production-sized processing. As a way of quantifying the temperature limits of the alloys, studies are aimed at understanding the mechanism(s) of the oxidation behavior of these alloys to facilitate the development of an analytical life prediction model.

The reason for the interest in ODS alloys is summarized in Fig. 1 which was derived from the data of Starr and Shibli[(1)] and compares the average 100kh stress rupture strength for all available wrought or cast high-temperature alloys with the theoretical maximum rupture strength that could be obtained if the strengthening mechanisms used were fully optimized. The diagram also indicates the range of strength required for ultra-supercritical steam conditions (relatively low temperature, high pressure) and for high-temperature heat exchangers for indirect-fired duty cycles (very high temperatures, relatively low pressures), from which it is seen that the capabilities of the current high-temperature alloys are marginal for both applications. The typical longitudinal stress rupture strength for ODS-FeCrAl alloys, also shown

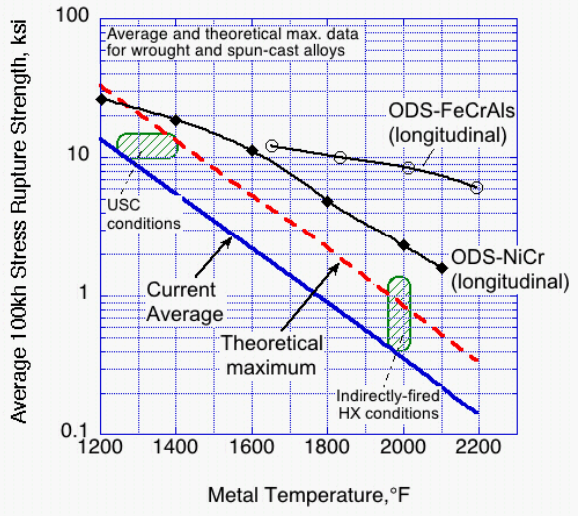

Fig. 1. Schematic comparison of the current average and theoretical maximum creep strength of current high-temperature alloys (after Starr and Shibli, 2000).

on the diagram, illustrates their strength advantage. Essentially, ODS alloys have potential for use to temperatures where otherwise ceramic materials would have to be considered. In addition, the ODS-FeCrAl alloys have excellent oxidation resistance due to the formation of a protective alumina scale, which confers excellent resistant to oxidation in air and steam, and to sulfidation. The efforts reported here are coordinated with those in Office of Fossil Energy's Advanced Research Materials (ARM) programs at the University of California at San Diego,[2] University of Liverpool,[3] and at Foster Wheeler Inc.[4] In addition, the efforts support a Vision 21 program conducted by Special Metals Inc. intended to increase the transverse creep rupture strength of an ODS ferritic alloy, MA956.[5] Approaches taken and results derived from efforts in other programs, in particular the European COST programs,[6] also are noted in planning the effort on this program. The alloys of interest are the commercial ferritic ODS alloys: MA956, MA956H, and PM2000; in addition an ORNL-developed alloy (ODS-Fe_3Al) is included, as well as an alloy used in an earlier European COST program for an externally-fired heat exchanger,[7] Dour Metal ODM751. A non-ODS, powder metallurgy-produced FeCrAl alloy (Kanthal APM) is included in the program as an oxidation comparator. The nominal compositions of these alloys are shown in Table 1.

Table 1. Compositions of the ferritic ODS alloys of interest (in wt%)

Alloy	Fe	Al	Cr	Mo	Ti	Dispersoid
ODS-Fe_3Al	Bal.	15.9	2.2		0.07	Y_2O_3
MA956H	Bal.	5.77	21.66		0.40	Y_2O_3
MA956	Bal.	4.46	19.64		0.39	Y_2O_3
PM2000	Bal.	5.5	20		0.5	Y_2O_3
ODM751	Bal.	4.5	16.5	1.5	0.6	Y_2O_3
Kanthal APM	Bal.	5.5	20		0.03	None

The focus of this paper is on the recent efforts on joining these alloys, as well as identification of their temperature limits in terms of oxidation behavior.

DISCUSSION OF CURRENT ACTIVITIES

JOINING OF ODS ALLOYS

The challenges faced in joining ODS alloys are that the processes used must avoid (1) redistributing the Y_2O_3 dispersed phase, which will float out of the alloy if it is fused, and (2) changing the grain size, shape, and orientation in the alloy microstructure. As a result, fusion processes are probably a last resort, although laser welding (which minimizes the size of the fused zone) has been used successfully for bonding sheet,[8] and brazing has been explored in the European COST-522 program for joining tubes.[6,9] Friction welding was shown earlier in this program[10] to result in distortion of the microstructure in the region of the joints formed on rod-shaped specimens, the effect of which was to degrade the creep strength in that area. Further investigation of a version of friction welding (inertia welding) reported here used tubes of MA956 and was intended to quantify the effect of the more symmetrical distortion of the microstructure expected for tube walls. Diffusion bonding using a TLP approach was successfully demonstrated in the HiPPS program for a Ni-Cr-based ODS alloy that forms a chromia scale.[11] Studies to extend this concept to the more difficult case of the alumina-forming FeCrAl ODS alloys is underway, and preliminary results are reported here. Further, progress has been made in a plasma-assisted diffusion bonding technique by the MER Corporation of Tucson, Arizona, and a detailed characterization of such joints also is reported.

Inertia welding of MA956 tubes: As-extruded, un-recrystallized tubes of MA956, with an outside diameter of 63.5 mm, and 7 mm wall thickness, were supplied to Interface Welding Inc., of Carson City, California for inertia welding trials. In this process, one section of tube is fixed in the hub of a large flywheel, while the section to which it is to be joined is attached to a rigid frame and aligned such that it will mate exactly with the section attached to the flywheel, as the flywheel is advanced. The process involves spinning up of the flywheel to a given speed, after which it is uncoupled from the drive and advanced with a known force until the tube attached to the flywheel encounters the rigidly-held section of tube in the frame. The energy from the momentum of the flywheel is dissipated by friction between the two sections of tube as the flywheel is held with the two tube sections in contact. The processing parameters were determined based on the integrity of the joints as judged in bend tests of coupons cut from the joined tubes. Sequences in the processing are illustrated in Fig. 2. The reproducibility of the parameters measured during joining was found to be excellent, and a number of samples of joined tube was produced for evaluation. A preliminary examination of the microstructure of the joint indicated that the deformation was confined to a relatively small zone near the joint, and that the demarcation between highly-deformed material and material exhibiting the normal microstructure following extrusion was very sharp. This is illustrated in Fig. 3, which shows a cross section at the tube outer surface near the joint for a sample that had been re-crystallized following joining. A more detailed examination of the joints by

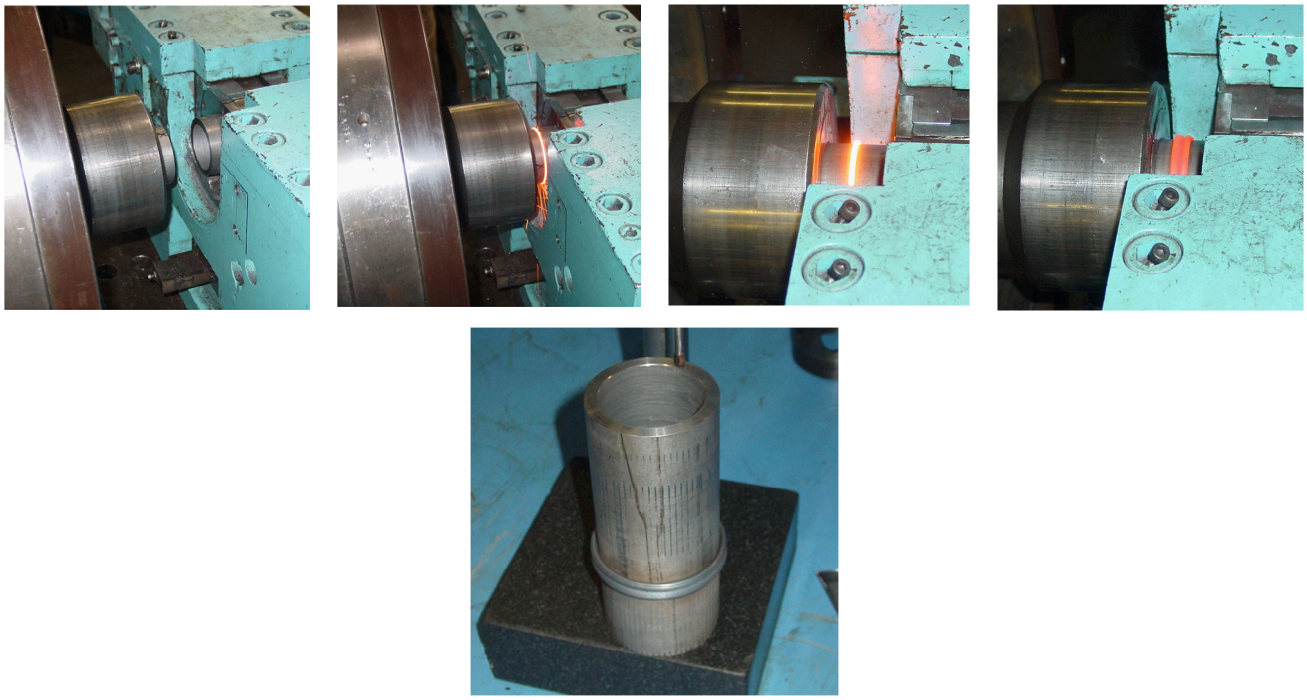

Fig. 2. Sequences in the inertia welding of a MA956 tube.

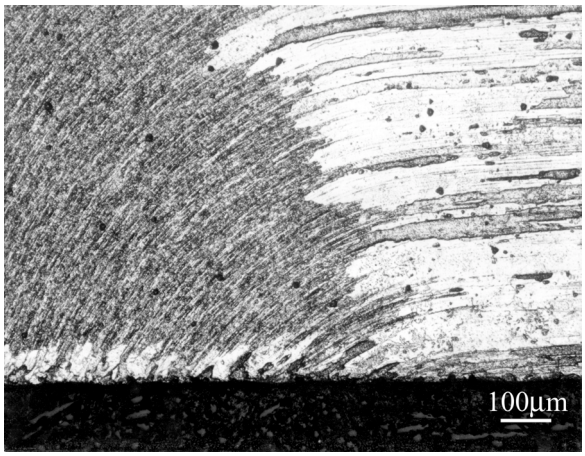

Fig. 3. Microstructure adjacent to joint in an inertia-welded MA956 tube, recrystallized after joining.

transmission electron microscopy (TEM) is in progress, and specimens are being prepared for creep testing of the joints

Plasma-assisted diffusion bonding: Figure 4 shows a cross section of a block of MA956 that was joined by plasma-assisted diffusion bonding (MER Corporation). The etched microstructure of the joint indicates that the bond line appears to be quite clean with essentially no indication of microstructural distortion along it. The appearance of grain continuity across the joint in places should not be interpreted to indicate that grain growth has occurred though the joint, since the alloy specimen had been re-crystallized before joining. The appearance is serendipitous. Examination of the bond by electron probe micro-analysis (EPMA) suggested that there was a collection of dark-appearing (in the back-scattered electron view) along the bond line that appeared to be enriched in Ti, Y, Al, and O, Fig. 5. A Y-enrichment might suggest some local accumulation of the yttria dispersoid as a result of localized melting, while Ti and Al enrichments may suggest accumulation of Ti-Al-rich particles that are normally present throughout the matrix of the

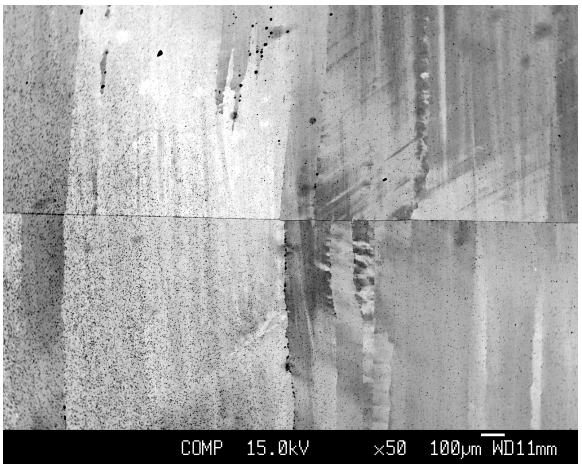

Fig. 4. Joint made by plasma-assisted diffusion bonding in MA956 (joined after recrystallization).

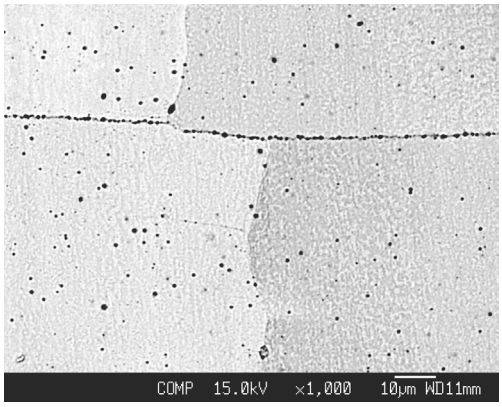

Secondary electron image

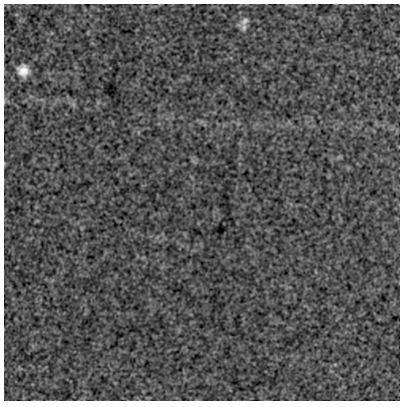

Oxygen X-ray map

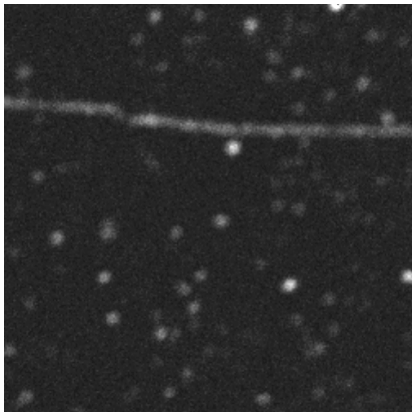

Titanium X-ray map

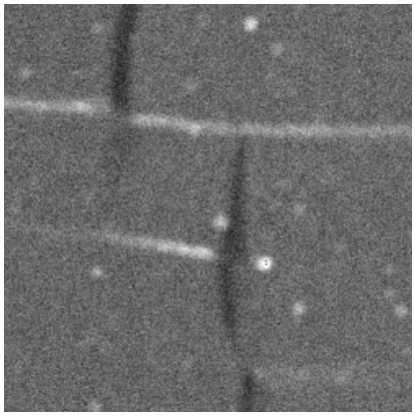

Yttrium X-ray map

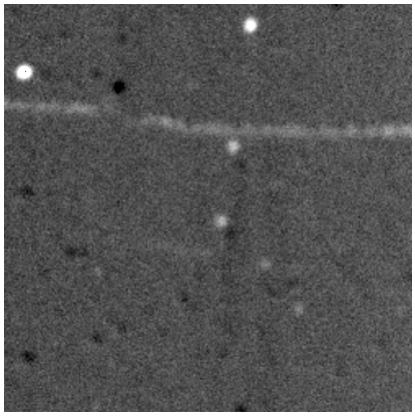

Aluminum X-ray map

Fig. 5. EPMA mapping of the center portion of the joint shown in Fig. 4.

alloy. The relative strength of the X-ray signals suggested that the particles along the bond line were predominately Ti-rich. Transmission electron micrographs of cross sections taken across the joint shown in Fig. 4 are shown in Figs. 6 and 7. In Fig. 6, the bond line has the appearance of an alloy grain boundary, which contains discrete particles but otherwise appears to be very clean. In Fig. 7, one of the larger particles is shown in detail to consist of a mixture of Al_2O_3 and TiC particles. While the sizes of these particles were similar to Ti-rich particles present in the original alloy microstructure, it is not known if the number of such particles along the bond line is similar to or greater than the population of particles in the original matrix.

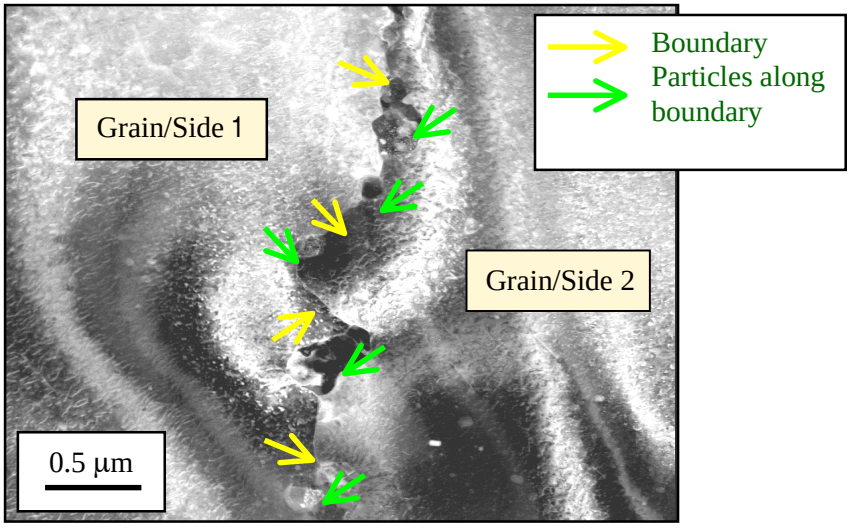

Fig. 6. Transmission electron micrograph across the bond shown in Fig. 5 (bond line runs top- bottom).

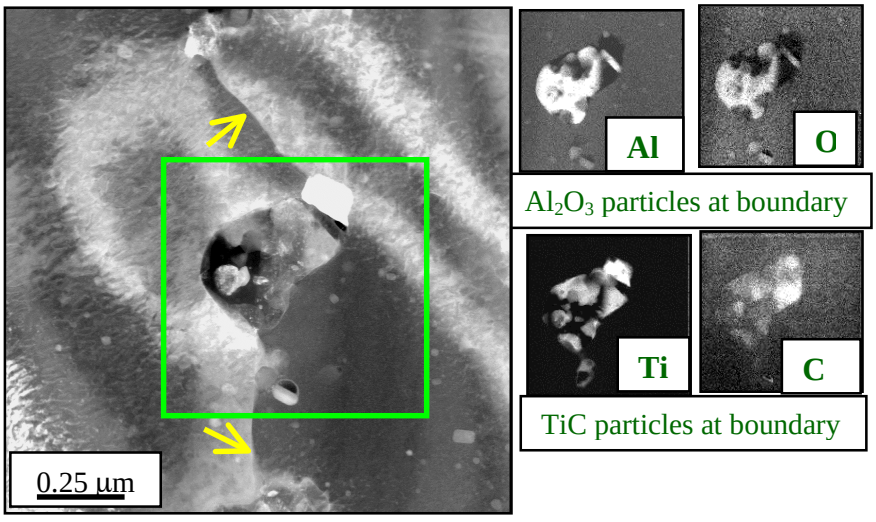

Fig. 7. Transmission electron micrograph of a particle in the bond line shown in Fig. 6 (bond line in indicated by arrows).

Transient liquid phase bonding: As part of a collaborative effort with the Energy & Environmental Research Center, Grand Forks, North Dakota (J. Hurley) and one of the original developers of TLP bonding in the HiPPS program (N. S. Bornstein), a proof-of-principle alloy for use as a transient liquid phase was melted and rolled into foil, and used in initial bonding trials for joining tubes of alloy MA956. A sample cross section of such a joint is shown in Fig. 8, which is an SEM back-scattered image. The bright-appearing particles in the interdiffusion zone on each side of the bond line are rich in the TLP alloy, and the data points indicated on the figure are locations where spot analyses were made using EPMA. The interest here is to develop joining conditions that allow the TLP to wet the surfaces to be joined, and for those surfaces to be in contact under conditions where there is sufficient time at temperature to allow diffusion bonding to occur. During this process, it is essential that the transient liquid phase diffuses away from the joint to the extent that any modification of the composition near the joint due to remaining TLP alloy phases is not detrimental to the mechanical properties. Detailed analysis of this joint by TEM is in progress. Results from the analysis will be compared with data from creep tests of specimens made from these joints and used to guide further development of the bonding conditions.

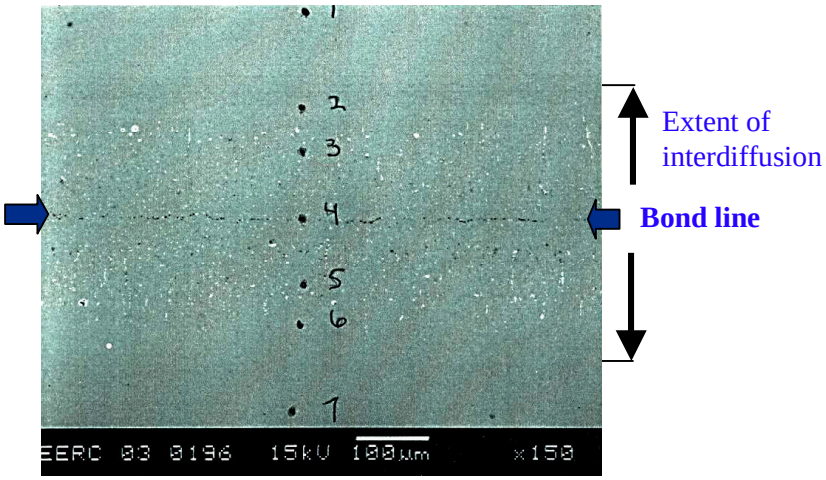

Fig. 8. Scanning electron micrograph of a TLP bond in alloy MA956.

TEMPERATURE LIMITS

It is expected that ODS alloys in service will be subjected to mechanical loading such that their rate of creep would be negligibly slow. As a result, the service life of these alloys is likely to be determined by their oxidation behavior. Further, these alloys form very thin alumina scales which grow very slowly and remain protective until the Al content in the alloy has been essentially exhausted, at which point a non-protective mode of oxidation will ensue (‘breakaway oxidation’). This means that the extent of oxidation attack during protective behavior cannot readily be assessed by the usual methods of measuring section thinning. As a result, there is need for a method for predicting the oxidation-limited lifetimes of such

alloys. Fortunately, for this class of FeCrAl alloys, the basis for such modeling is relatively straightforward since there are several simplifying factors or assumptions involved:

- these alloys form essentially single-phase scales of alumina that are uniform in thickness;
- there is negligible internal attack; and
- the Al concentration gradient in the alloy remains flat until very near the end of life.

As a result, it is possible simply to equate the oxidation lifetime to the rate of consumption of the available Al to form the oxide scale,[12] so that:

Oxidation-limited lifetime = (Al available for oxidation) / (oxidation rate)

The oxidation kinetics of these alloys, in terms of total mass change (total oxygen consumed), have a characteristic shape as indicated in Fig. 9. For the purposes of modeling, the oxidation behavior has been described as involving three stages, defined as:

Stage 1, which involves initial, transient, oxidation is very short for these alloys at the temperatures of interest, and so is ignored for the purposes of modeling.

Stage 2, which involves growth of the oxide according to a parabolic rate law; and

Stage 3, which involves a period of linear mass gain as result of continuing oxide growth, as well as spallation of some of the scale.

As shown in Fig. 9, Stage 3 ends with a rapid increase in the total mass gain due to the formation of a non-protective scale, as breakaway oxidation ensues.

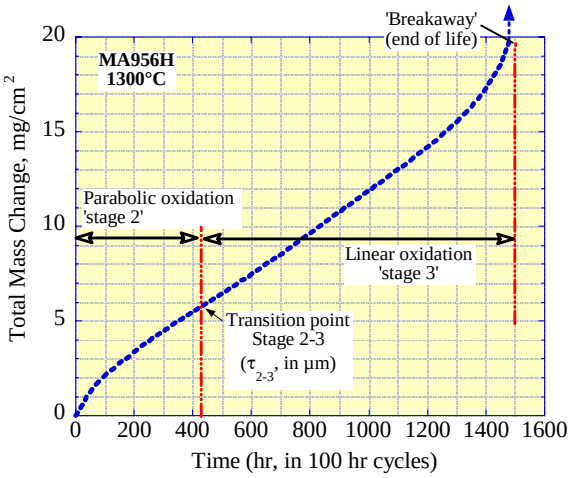

Fig. 9. Typical form of the oxidation kinetics of ferritic ODS alloys.

The current expression of the model based on this approach is:

$$t_b = \{[S*10^{-4}*\rho_A*A_\tau*e^{-Q\tau/(1.987*T)}]^2/(3600*A_2*e^{-Q2/(1.987*T)})\} + \{[1/(3600*M)*(V/A)*(\rho_M/(A_3*e^{-Q3/(1.987*T)}))*$$

$$[(C_{Bo}-C_{Bb}) - M*S*10^{-4}*(A/V)*(\rho_A/\rho_M)*A_\tau*e^{-Q\tau/(1.987*T)}]\} \text{ hours}$$

This is a simple, deterministic, algebraic expression for which the input required consists of:

(a) data about the alloy (density: ρ_M; initial aluminum content: C_{Bo}; Al content at which failure occurs: C_{Bb});

(b) about the oxide (density:ρ_A; constants based on oxide and alloy stoichiometry: M, S); and

(c) alloy oxidation descriptors (essentially Arrhenius data for the various stages of oxidation: A_2, Q_2; A_3, Q_3; A_τ, Q_τ).

Given these data for a given alloy, the only input required to predict oxidation-limited lifetime is the metal temperature (T), and the component size (represented by the volume of the component divided its surface area, V/A). This parameter is useful, since for a tube V/A = d/4, were d is the wall thickness. The oxidation parameters were generated from long-term oxidation exposures in which specimens were taken to failure. Note that Stage 3 kinetics are only experienced for oxide scale thicknesses greater than approximately 20 μm, and that at the lower temperatures of interest (1000, 1100°C), such scale thicknesses are only obtained after many thousands of hours of exposure. In addition, the value of C_{Bb} must be measured experimentally, which requires exposing specimens to failure and then being able to remove them from test immediately upon failure before they are consumed by breakaway oxidation. Using the oxidation data and values of the C_{Bb} measured to date, the lifetime model was exercised for a particular alloy, MA956H, to predict the oxidation-limited lifetimes as a function of wall/section thickness (V/A) and temperature, with the results shown in Fig. 10. Figure 11 shows the correspondence of these predictions with experimentally-observed lifetimes for this alloy: even though the oxidation lifetime axis is logarithmic, the predictions appear to be reasonable.

Because this alloy oxidizes very slowly, data for 1100°C are sparse: the one specimen so far oxidized to failure exhibited a life of 23,400 hours. Figure 12 shows similar predictions and experimentally-observed lifetimes for alloy MA956, which has an oxidation rate significantly faster than MA956H. For this alloy, there are several experimental data points at 1100 and 1200°C, which allow the suggestion that the predictions given by this simple model are reasonable, if optimistic, for temperatures in the range of 1100 to 1300°C. On this basis, and using values of C_{Bb} measured at only two temperatures, the model was exercised to provide comparative lifetimes as a function of temperature and section thickness for all of the ODS alloys of interest. Predictions for 1100°C are shown in Fig. 13, which indicates that all of the alloys (except MA956) are expected to exhibit reasonably similar lifetimes for the thicker sections (V/A > 0.4),

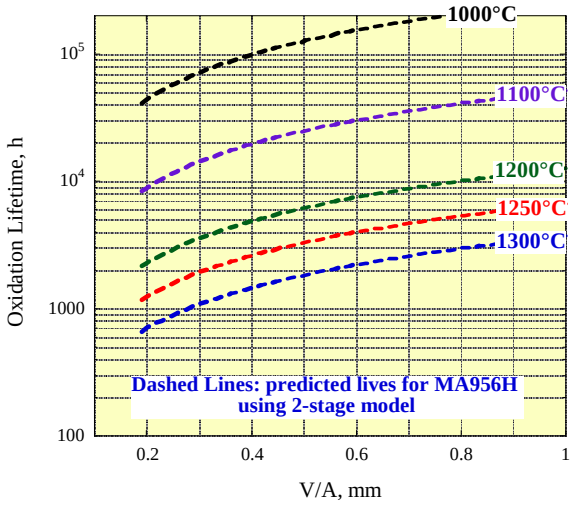

Fig. 10. Predicted oxidation lifetimes for alloy MA956H.

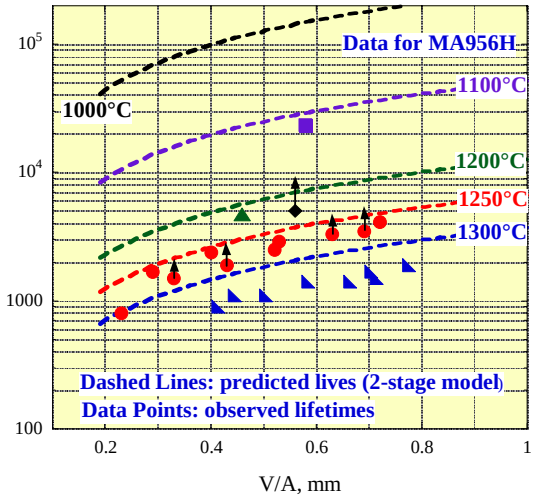

Fig. 11. Comparison of predicted and observed oxidation lifetimes for alloy MA956H.

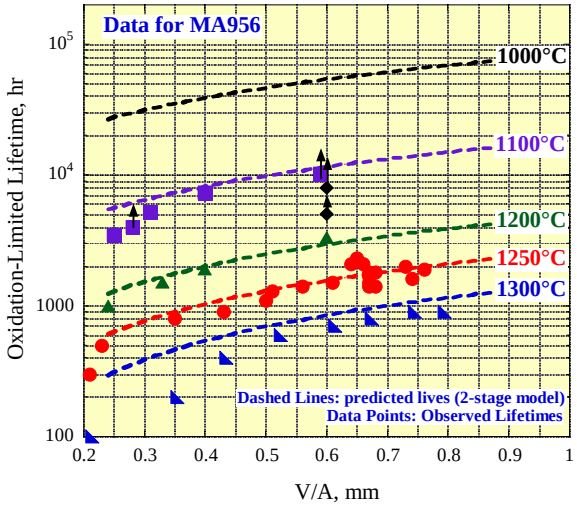

Fig. 12. Comparison of predicted and observed oxidation lifetimes for alloy MA956.

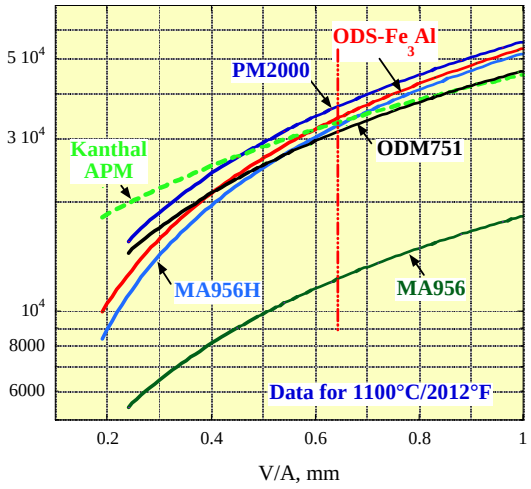

Fig. 13. Comparison of predicted oxidation lifetimes for all the ODS alloys of interest at 1100°C (note that the vertical line denotes the V/A value for a tube of 2.5 mm thickness)

while there is some differentiation among the alloys for thinner sections. Note also that in Fig. 12 there is an increasing divergence between the predicted and the observed lifetimes as the value of V/A decreases from 0.5 to 0.2. Presumably, there is some feature of thinner sections that is not treated correctly by the model.

The difference in oxidation rate, hence oxidation-limited lifetime, between alloys MA956 and 956H is considered surprising since the only major difference in the nominal compositions of these alloys is in Al content, which would be expected to change the total oxidation-limited lifetime (difference in Al

reservoir), but would not have been expected to influence the oxidation rate. Examination of the detailed compositions of these two alloys indicated a higher level of "free" Ti in MA956 (0.3 compared to 0.2 atomic %), where free Ti is that in excess of the amount required to form compounds with the C and N present in the alloy. Incorporation of Ti into the alumina scales formed on ODS-FeCrAl alloys has been shown in some cases to modify the rate of scale growth; however, results for variants of PM2000 indicated an *increase* in life with an increase from 0 to 0.4 at% Ti,[13] which tends to discount the influence of Ti in the current results. TEM cross sections of the scales formed on these two alloys are compared in Figs. 14 and 15 for samples oxidized for 100 hours at 1200°C in air. Both formed scales that exhibited the grain structure expected from reactive element doping[14] (by yttrium in this case) and, while Y was found to be enriched at the oxide grain boundaries as expected, and Ti was enriched at the oxide metal interface, it was not possible to make quantitative comparisons of such enrichments between the two alloys. Other features found in the oxide scale on MA956, shown in Fig. 15, were large inclusions identified as TiC particles, and particles containing Y, Ti, Si, and C (but, apparently, no O). The latter particle in the cross section shown is oriented parallel to the major oxide grain boundaries, so that it might be capable of acting as a rapid diffusion path for oxygen, hence increasing the oxidation rate. Also, it appears to have caused some mechanical disruption of the oxide scale with an obvious void or crack present in the scale above it.

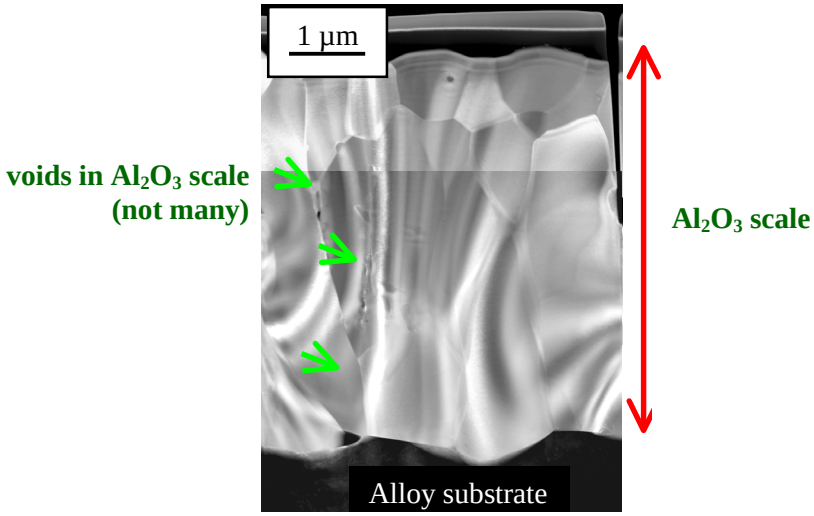

Fig. 14. TEM of a cross section of the oxide scale formed on alloy MA956H oxidized for 2h at 1200°C in air, showing the expected large, columnar-grained structure.

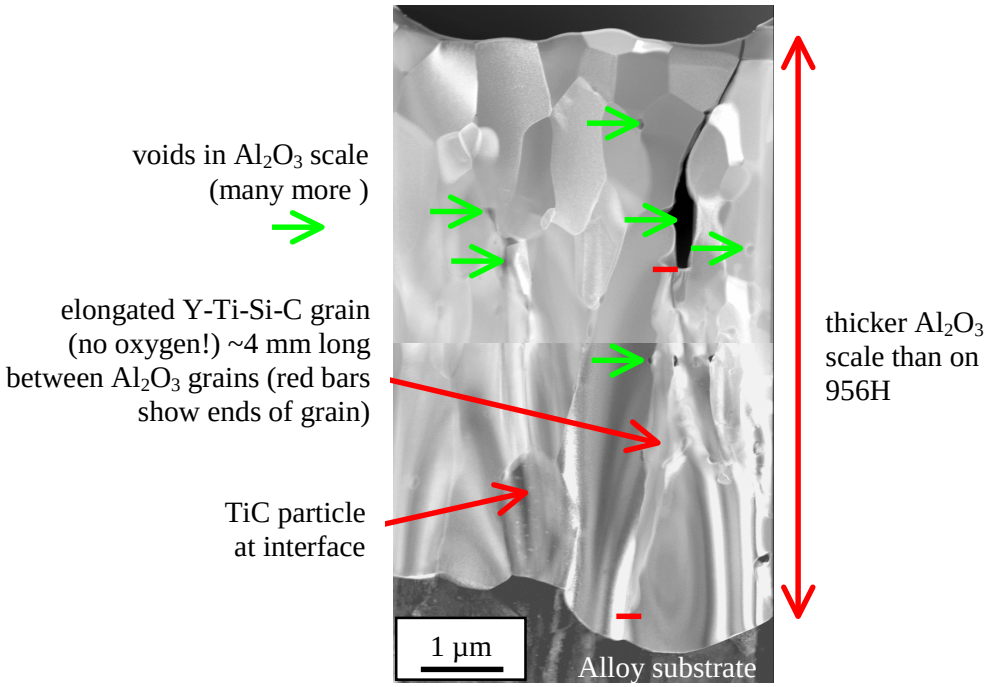

Fig. 15. TEM of a cross section of the oxide scale formed on alloy MA956 oxidized for 2h at 1200°C in air, showing thicker scale than 956H, and inclusions in the scale.

EFFECT OF SPECIMEN SHAPE

One of the obvious shortcomings of the current life prediction model is that it over-predicts lifetime, whereas such predictions should be conservative. Observations from the oxidation exposure tests suggested that the oxidation lifetime, that is, the time to failure, may be influenced by the shape of the specimen used in the laboratory tests. The specimen shapes typically are parallelepipeds or discs of various lengths and thicknesses. While the parameter V/A is a shape factor of sorts, it did not appear to account sufficiently for the difference between predicted and observed lifetimes. Potential sources of over-prediction of the oxidation lifetime include:

- an under-representation of the actual oxidation rates in Stages 2 and 3;
- assumption a larger reservoir of available Al than experienced in practice: this could arise though the use of too low a value of the minimum Al content (C_{Bb}), or from the development of a gradient in the Al concentration profile near the specimen surfaces toward the end of life[15]; and
- lack of a treatment for the acceleration in Al consumption immediately before break away occurs.

These considerations led to the study of the effect of specimen shape on oxidation life involving two sizes of parallelepiped, a disc, and a cylinder. The dimensions were chosen such that the parallelepipeds and the discs had the same thickness; the smaller parallelepiped had the same volume as the disc, as did the standard parallelepiped and the cylinder; and the cylinder and the small parallelepiped had the same

surface area. Note that the V/A parameter was the same for the parallelepipeds, so that it did not discriminate between them.

Figure 16 shows the total mass gain-time curves at 1250°C for the different shapes. In particular, the disc exhibited a longer life than did both the parallelepipeds, presumably reflecting its larger V/A ratio. Also, the larger parallelepiped failed first, significantly earlier than the small parallelepiped. For the disc and parallelepipeds the color of the alumina scale changed from grey to dull pink before any breakaway oxidation was observed, confirming that the available Al in the alloy had been depleted significantly. The large parallelepiped failed at a corner, as shown in Fig. 16, and the demarcation between the protective and the failed oxide was very sharp, as shown in the SEM topograph in Fig. 17a. A cross section of the non-failed corner adjacent to the failed corner shown in Fig. 17b indicated that the protective oxide scale was of essentially uniform thickness around the end of the specimen, with no signs of imminent failure: note also a cluster of large voids (possibly Kirkendall voids) in the center of the specimen thickness near the end, together with internal precipitates, the elongated ones of which were TiN. In contrast, the small parallelepiped appeared to fail essentially at all four corners simultaneously, after which the growth of a non-protective scale proceeded rapidly across the specimen surface in an essentially symmetrical way.

Consideration of the reasons for the early failure of the large parallelepiped led to examination of the conditions prevailing as the point of breakaway oxidation is approached. If a flat Al concentration profile is assumed to persist throughout the oxidation lifetime of the specimen, the point on the alloy surface that will be the first to fall below C_{Bb} and experience breakaway oxidation will that which represents the

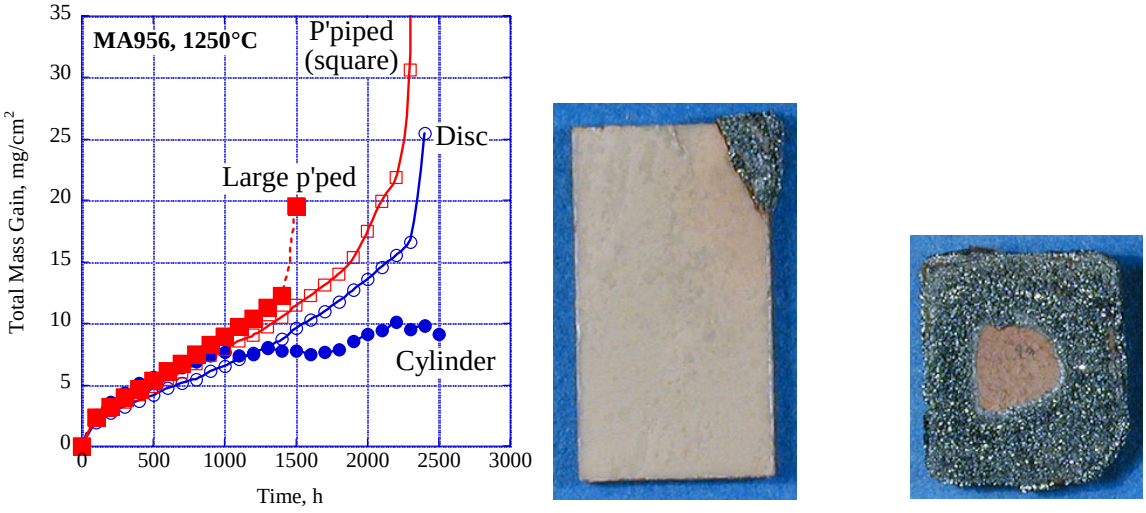

(a) **(b)** **(c)**

Fig. 16. Oxidation behavior of different specimen shapes, MA956, 100h cycles at 1200°C in air. (a) oxidation kinetics, 100h cycles at 1250°C; (b) large parallelepiped showing failure at one corner; (c) small parallelepiped showing symmetrical progression of breakaway oxidation.

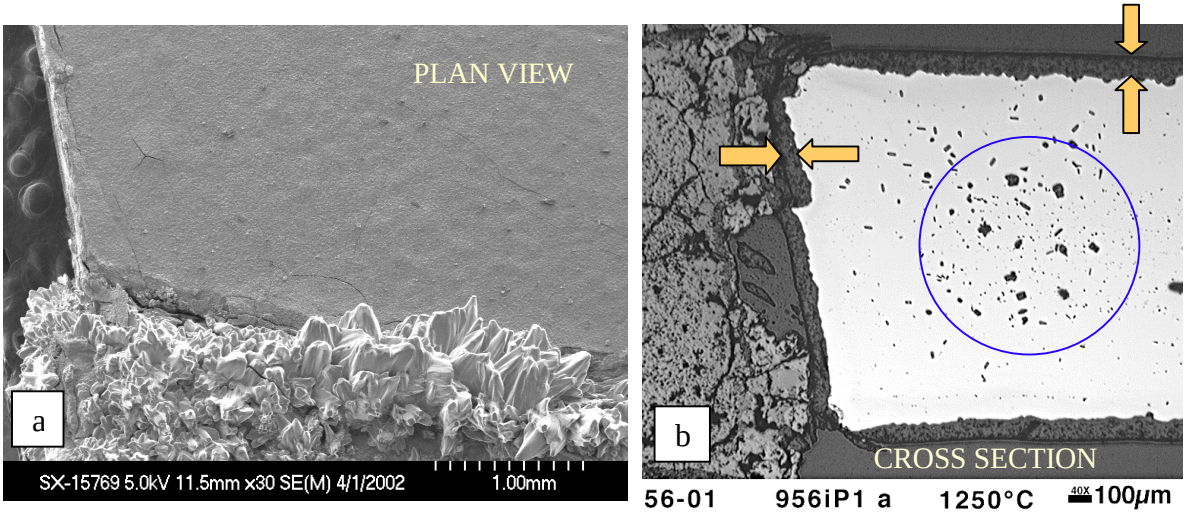

Fig. 17. Mode of failure of a long parallelepiped specimen of MA956 (a) plan view of the corner at which breakaway initiated; (b) cross section of the adjacent corner: the scale shows no sign of imminent breakaway behavior.

longest distance that Al from the center of the reservoir has to travel. With a flat Al concentration profile, the center of that reservoir may be considered to be the center of the alloy thickness, so that the surface of a sphere that touches four sides of the parallelepiped (see Fig. 18) represents the minimum diffusion path length to any surface. The radius of that sphere is half the thickness of the parallelepiped (or d/2), while the distance to an edge is 0.7d, and the distance into the corner is 0.87d. These distances are shown in Table 2, in which w is width; and l is length. Interestingly, these considerations do not suggest a reason for the difference in oxidation lifetimes of the two parallelepipeds (same thickness). This is possibly an indication that the assumption that a flat Al concentration profile persists until breakaway occurs is not sound and, in that case, the center of the Al reservoir would be the center of mass. The longest diffusion distance in a parallelepiped is that from the center of mass to a corner. The formulation for this distance, listed in Table 2, involves all of the dimensions of the parallelepiped, and so holds some promise for discriminating between the behavior parallelepiped sizes.

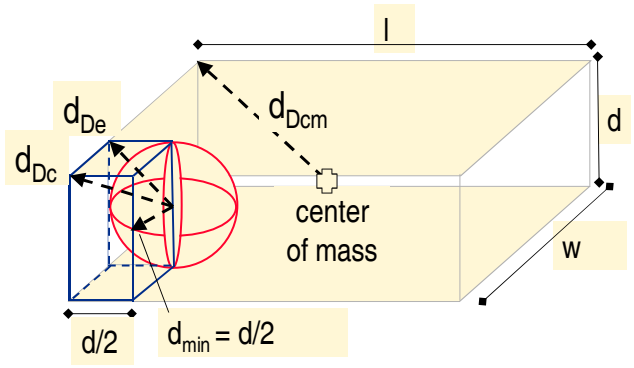

Fig. 18. Schematic representation of diffusion lengths in a parallelepiped.

Table 2. Suggested shape factors: diffusion lengths

Shape	Edge d_{De}	Corner d_{Dc}	Center of Mass d_{Dcm}
P'piped	$0.707 \times d$	$0.866 \times d$	$0.5 \times \text{sqrt}\ (l^2 + w^2 + d^2)$
Cylinder	—	$0.707 \times \text{diam}$	$0.5 \times \text{sqrt}\ (l^2 + \text{diam}^2)$
Disc	$0.707 \times d$	$0.707 \times d$	$0.5 \times \text{sqrt}\ (d^2 + \text{diam}^2)$

CONCLUSIONS

The results reported indicate that progress has been made in the joining of ODS alloys, as well as in determining the temperature limits of this class of alloy. Three routes are being evaluated for joining these alloys: *inertia welding*, where interest is in controlling and understanding the microstructural distortion caused by the process; *plasma-assisted diffusion*, which appears capable of producing clean joints and where interest is centered on determining the source of alumina-titanium carbide particles along the bond line and their influence on mechanical properties: and thirdly *transient liquid phase bonding*, for which the major questions concern the amount of TLP alloy remaining near the bond line, and its effect on alloy properties. The effort to determine the temperature limits of these alloys has involved generating oxidation data for all the available ODS-FeCrAl alloys, including running exposures for very long times until oxidation failure occurs. In addition, an initial working model for prediction of the oxidation-limited lifetime has been developed that appears to give reasonable predictions for alloy lifetimes over the temperature range 1100 to 1300°C. A major concern with this model at present is the fact that it over-predicts the lifetimes of specimens exposed to failure in the laboratory, and analysis is continuing to provide a mathematical description of specimen shapes that would cause the model to better discriminate among different shapes. Nevertheless, given that the predictions of the model are reasonable, it indicates that lifetimes of between 30,000 and 70,000 hours at 1100°C would be expected for typical tube sizes, with wall thicknesses ranging from 2.5 to 6.4 mm.

ACKNOWLEDGMENTS

This research was sponsored by the Fossil Energy Advanced Research Materials (ARM) Program, U.S. Department of Energy, under contract DE-AC05-96OR22464 with UT-Battelle LLC. Program of the U.S. Department of Energy. Mr. L. D. Chitwood was responsible for the oxidation lifetime tests; Mr. L. R. Walker carried out the electron microprobe analyses; and Ms. D. W. Coffey and Dr. K. L. More were responsible for preparing the TEM images.

REFERENCES

1. F. Starr and I. A. Shibli, "Fundamental issues in the development of austenitic and Ni-based alloys for advanced supercritical steam and high-temperature indirect-fired gas turbines," pp. 459–471 in *Proc. Fifth Intl. Charles Parsons Turbine Conference: Advanced Materials for 21st Century Turbines and Power Plant,* A. Strang, W. M. Banks, R. D. Conroy, G. M. McColvin, J. C. Neal, and S. Simpson, Eds., IOM Communications Ltd., Book No. 736 (2000).
2. B. Kad, J. Heatherington, I. G. Wright, and V. K. Sikka, "Optimization of ODS FeCrAl and Fe_3Al properties," *Proc. 17th Annual Conference on Fossil Energy Materials*," Baltimore, Maryland, April 2003.
3. A. R. Jones, J. Ritherdon, and D. J. Prior, "Reduction of defect content in ODS alloys," ibid.
4. J. L. Blough and W. W. Seitz, "Fireside corrosion testing of candidate superheater tube alloys, coatings, and claddings-Phase III," ibid.
5. M. A. Harper, "Improved ODS alloy for heat exchanger tubing," *Proc. 16th Annual Conference on Fossil Energy Materials*," Baltimore, Maryland, April 2002.
6. F. Olsson, S. A. Svensson, and R. Duncan, "Externally-fired gas turbine cycles with high-temperature heat exchangers utilizing Fe-based alloy tubing," pp. 139–153 in *Proc. 15th International Plansee Seminar*, G. Kneringer, P. Rodhammer, and H. Wildner, Eds., Plansee Holding AG, Reutte (2001).
7. F. Starr, A. R. White, and B. Kazimierzak, in *Materials for Advanced Power Engineering 1994*, D. Coutsouradis, et al., Eds. (Kluwer Academic Publishers, 1994) pp. 1393–1412.
8. C. Brown, E. Verghese, D. Sporer, and R. Sellors, "PM2000 honeycomb structures," Paper 98-GT-565, presented at the *43rd AMSE Gas Turbine and Aeroengine Technical Congress*, Exposition, and Users Symposium, Stockholm, Sweden, June 2–5, 1998.
9. S. Holmstrom, M. Siren, L. Heikinheimo, P. Auerkari, J. Varmavuo, and R. Saarinen, "Performance of an iron-based ODS alloy in a boiler environment," pp. 769–777 in *Materials for Advanced Power Engineering 1998*, LeComte-Beckers, F. Schubert, and P. J. Ennis, Eds., Forschungszentrum, Zentralbibliothek, 1998.
10. P. L. Threadgill, *Friction Welding of an Fe_3Al-based ODS Alloy*, Report No. ORNL/Sub/97-SX373/01, July 1998. See, also, B. J. Inkson and P. L. Threadgill, "Friction Welding of Fe-40Al Grade 3 ODS Alloy," *Mat. Sci. and Eng*., **A258**, 313–318 (1998).
11. D. J. Seery and J. Sangiovanni, "Engineering development of a coal-fired high-performance power generating system," Paper No. 1.7 in *Proc. of the Advanced Coal-Based Power and Environmental Systems'98 Conference*, Morgantown, West Virginia, July 21–23, 1998, DOE/FETC-98/1072.
12. W. J. Quadakkers, K. Bongartz, F. Schubert, and H. Schuster, in *Materials for Advanced Power Engineering 1994*, D. Coutsouradis, et al., Eds. (Kluwer Academic Publishers, 1994) pp. 1533–1542.

13. W. J. Quadakkers, D. Clemens, and M. J. Bennett, “Measures to improve the oxidation limited service life of Fe-based ODS alloys,” pp.195–206 in S. B. Newcomb and J. A. Little, (Eds.), *Microscopy of Oxidation 3*, Institute of Metals, London, U.K. (1997).
14. B. A. Pint, “Study of the reactive element effect in ODS iron-base alumina-formers,” *Mater. Sci. Forum*, **251–254**, 397–404 (1997).
15. B. A. Pint, L. R. Walker, and I. G. Wright, “Characterization of the breakaway Al content in alumina-forming alloys,” *Proc. 5th International Conference on the Microscopy of Oxidation*, Limerick, Ireland (2002).